Simulation study of a Squall line hailstorm using High-Resolution GRAPES-Meso with a modified Double-Moment Microphysics scheme

Zhe Li[1,2], Qijun Liu[1,2], Xiaomin Chen[3], Zhanshan Ma[1,2], Jiong Chen[1,2], and Yuan Jiang[1,2]

[1]National Meteorological Center, Beijing, 100081, China
[2]Numerical Weather Prediction Center of China Meteorological Administration, Beijing, 100081, China
[3]Chongqing Meteorological Service, Chongqing, 401147, China

Correspondence to: Zhe Li (liz@cma.gov.cn)

Abstract. This study uses the high-resolution GRAPES_Meso (the mesoscale version of the Global/Regional Assimilation and Prediction System) to simulate a severe squall line hailstorm in Shandong province. The accumulated precipitation, radar reflectivity, and cloud hydrometeor properties simulated using a modified double-moment microphysics scheme are compared with observation. Results show that simulations captured the basic character of this squall line hailstorm. The simulated accumulation precipitation and radar reflectivity are comparable with the observation. The cross-section of the dynamic, microphysical, and radar reflectivity structures of the simulated hailstorm was analyzed. The simulated hailstorm has shown a reasonable result in both macrostructure and micro hail production rates. The development of the simulated hailstorm is consistent with the conceptual model of hailstorm evolution. Results imply the ability of high-resolution GRAPES_Meso on forecasting hailstorm.

1 Introduction

Hailstorm is one of the severe disaster weathers for agricultural countries like China, which occurs mostly in spring and summer. Hailstorm damages crops in the farmland, hailstorm may also destroy transportation, electricity, and communication equipment in the city. In extreme cases, hailstorms can even threaten people's life. Because of the destructive power, hailstorm is concerned by recent researchers. In Europe, the hail damage increased during the late 1900s (Mohr and Kunz, 2013; Kunz et al., 2009). In Canada, Cao (2008) investigated a robust ever-increasing frequency of severe hailstorms based on damage data and pointed out an increase in hail damage there. In China, studies show that although hailstorm frequency is decreased during the past 50 years (e.g. Fu et al. 2011, Zhao et al. 2019), the average single hailstorm duration increased (Zhao et al. 2019).

Hail is defined as a large ice particle with a diameter larger than 5 mm. Hail is formed associated with very strong updrafts in severe convective storms. Liquid droplets are carried by the strong updrafts into extremely cold areas and freeze in the form of ice balls. Tiny ice crystals that work as hail nucleus comes from graupel or freezing droplets (Browing et al. 1963; Bringi

30   et al. 1986; Hubbert et al. 1998). Distinguished by the surface temperature of a hailstone, the growth of hail can be separated into dry and wet growth (Lesins and List 1986; Garcia-Garcia and List 1992). In wet growth, the hail nucleus is in a region where the air temperature is closed to the hail surface. Therefore, the supercooled water droplet does not immediately freeze around the nucleus. In dry growth, the air temperature is well below freezing, and the water droplet immediately freezes as it collides with the hail nucleus. Graupel can convert to hail inappropriate situations (Ilotoviz et al. 2016; Vié et al. 2016). Note

35   that as mentioned by Hu and He (1988), the conversion rate of graupel to hail is the most important source for hail formation, compared to other processes. Meanwhile, researchers pointed out that strong vertical wind shear is favorable for hail formation (Das, 1962; Dennis and Matthew, 2017).

However, as the absence of observation and the sophisticated microphysical processes during hail formation and growth, the accurate forecasting of the position and time of hailstorm forecasting is extremely challenging (Knight and Knight 2015; Luo

40   et al. 2017). Therefore, hail is not a common forecaster in most operational numerical weather prediction (NWP) models (e.g. Sokol et al. 2014). Despite the above difficulties, the efforts of improving hail simulation never stopped. Moore and Pino (1990) use a diagnostic/prognostic sounding analysis package to add operational forecasters and found that this method helps estimate the maximum hail diameter. Jewell and Brimelow (2009) use a one-dimensional model to predict hail size and coupled the one-dimensional model to a regional model (Brimelow and Reuter, 2009). Adams-Selln and Zeigler (2016) use

45   the same approach to successfully forecast a reasonable hail size. Chatterjee et al. (2008) modified a cloud microphysics scheme in the regional model for simulating hailstorms. Yang et al. (2011) study the aerosol effects on hailstorms and found that increasing aerosol might decrease surface accumulated precipitation. Luo et al. (2014) use multimoment microphysics schemes to predict hailstorm explicitly. Labriola et al. (2019) adopt an explicit ensemble method to predict hail and analysis hail growth with different microphysics schemes.

50   The Global/Regional Assimilation and Prediction System (GRAPES) is an operational numerical weather prediction system that has been developed in the China Meteorological Administration since 2000 (Chen et al., 2012; Ma et al., 2018, 2020; Chen et al., 2020). The mesoscale version of GRAPES (GRAPES_Meso) is an important component of the GRAPES. GRAPES_Meso was first put into operational application in the National Meteorological Center in 2006 and has been continuously developed since then. The operational products of GRAPES_Meso are provided to meteorological agencies at

55   all levels in China ever since. Not only being used as an operational model since 2006 (Xu et al. 2017), GRAPES_Meso is also a suitable tool for scientific investigation (e.g., Deng et al; Huang et al. 2012; Wang et al. 2014; Wan et al. 2015; Wang et al. 2017). The high-resolution version of GRAPES_Meso (horizontal resolution of 3km) has been developed in 2015.

The purpose of this study is to test the ability to forecast a hailstorm using high-resolution GRAPES_Meso with a modified double-moment and to evaluate the performance based on comparisons of simulation results and observational data. The

60   modified double-moment microphysical scheme is described in Section 2. A brief overview of the squall line hailstorm and experimental design are shown in Section 3. Results are shown in Section 4. Summary and discussion are provided in Section 5.

2 Brief description of the double-moment microphysics scheme

The double-moment mixed-phase scheme developed from the convective and stratus cloud (Hu and He, 1988; Hu and Yan,
65 1986) using a box model. It was embedded in regional and global scale models for weather forecasting and scientific
research (e.g., Zhang and Liu 2006; Shi et al. 2015; Ma et al. 2018, 2020). Li et al. (2018, 2019a, 2019b) tested the
performance of this double-moment microphysics scheme in multi-scale models and improved its mixed-phase
microphysical processes. The basic version of the double-moment microphysics scheme predicts the mass mixing ratios of
cloud (Q_c), rain (Q_r), ice (Q_i), snow (Q_s), graupel (Q_g) and the number concentrations of rain (N_r), ice (N_i), snow (N_s) and
70 graupel (N_g). Detailed descriptions of this double-moment microphysics scheme can be seen in Hu and Yan (1986), Hu and
He (1988), Chen et al. (2007).

A modified version of this double-moment microphysics scheme which contains the prediction of hail mixing ratio (Q_h), hail
number concentration (N_h), and associated microphysical processes are developed to investigate hailstorm in this study.
Related equations are shown below:

75
$$\lambda_h^{-1} \approx \sqrt[3]{q} + \frac{D_*^2}{18\sqrt[3]{q}} - \frac{D_*}{3}, \tag{1}$$

Where λ_h (cm) is the slope parameter for hail, D_* (cm) is the minimum diameter of hail, which is 0.5, q is a temporary
variable calculated in Eq.（2）:

$$q = -\frac{2D_*}{27} + \frac{Q_h}{6A_{mh}N_h}, \tag{2}$$

Where A_{mh} is the fall speed parameter of group hail particles, which is 0.471 g cm⁻³.

80
$$\overline{V}_h \approx \sqrt{\frac{\rho_0}{\rho}} A_{vh} \lambda_h^{-0.8} \frac{[\beta_h^{3.8} + 3.8\beta_h^{2.8} + 10.64\beta_h^{1.8} + 17.84(0.8\beta_h + 1)]}{[\beta_h^3 + 3\beta_h^2 + 6\beta_h + 6]}, \tag{3}$$

Where $\overline{V}_h$ (cm s⁻¹) is the mean fall speed of hail, ρ_0 (g cm⁻³) is air density at the freezing point, ρ (g cm⁻³) is the air density,
A_{vh} is fall speed parameter of single hail particle, which is 810 cm⁰·² s⁻¹, β_h is a temporary variable ($\beta_h = \lambda_h D_*$).

Collision, autoconversion, melting and sublimation processes of hail are considered in this modified double-moment scheme.
Collision processes contain hail collision with cloud, rain, ice, snow, and graupel as follows:

85
$$C_{ch} \approx \frac{\pi}{4} A_{vh} \rho Q_c \overline{E}_{ch} N_h \lambda_h^{-2.8} [(\lambda_h D_*)^{2.8} + 2.8(\lambda_h D_*)^{1.8} + \Gamma(3.8)(0.8\lambda_h D_* + 1)] \sqrt{\frac{\rho_0}{\rho}}, \tag{4}$$

$$C_{rh} = \frac{\pi}{4} \rho |\overline{V}_h - \overline{V}_r| \overline{E}_{rh} Q_r N_h \lambda_h^{-2} [(\lambda_h D_*)^2 + 2\lambda_h D_* + 2 + 8\frac{\lambda_h}{\lambda_r}(\lambda_h D_* + 1) + 20(\frac{\lambda_h}{\lambda_r})^2], \tag{5}$$

$$C_{ih} = \frac{\pi}{4} \rho |\overline{V}_h - \overline{V}_i| \overline{E}_{ih} Q_i N_h \lambda_h^{-2} \left[(\lambda_h D_*)^2 + 2\lambda_h D_* + 2 + 8\frac{\lambda_h}{\lambda_i}(\lambda_h D_* + 1) + 20\left(\frac{\lambda_h}{\lambda_i}\right)^2\right], \tag{6}$$

$$C_{sh} = \frac{\pi}{4} \rho |\overline{V}_h - \overline{V}_s| \overline{E}_{sh} Q_s N_h \lambda_h^{-2} [(\lambda_h D_*)^2 + 2\lambda_h D_* + 2 + 8\frac{\lambda_h}{\lambda_s}(\lambda_h D_* + 1) + 20(\frac{\lambda_h}{\lambda_s})^2], \tag{7}$$

$$C_{gh} = \frac{\pi}{4} \rho |\overline{V}_h - \overline{V}_g| \overline{E}_{gh} Q_g N_h \lambda_h^{-2} [(\lambda_h D_*)^2 + 2\lambda_h D_* + 2 + 8\frac{\lambda_h}{\lambda_g}(\lambda_h D_* + 1) + 20(\frac{\lambda_h}{\lambda_g})^2], \tag{8}$$

90
$$NC_{rh} = \frac{\pi}{4} \rho |\overline{V}_h - \overline{V}_r| \overline{E}_{rh} N_r N_h \lambda_h^{-2} [(\lambda_h D_*)^2 + 2\lambda_h D_* + 1 + 2\frac{\lambda_h}{\lambda_r}(\lambda_h D_* + 1) + 2(\frac{\lambda_h}{\lambda_r})^2], \tag{9}$$

$$NC_{ih} = \frac{\pi}{4}\rho|\overline{V}_h - \overline{V}_i|\overline{E}_{ih}N_iN_h\lambda_h^{-2}[(\lambda_hD_*)^2 + 2\lambda_hD_* + 2 + 4\frac{\lambda_h}{\lambda_i}(\lambda_hD_* + 1) + 6(\frac{\lambda_h}{\lambda_i})^2], \tag{10}$$

$$NC_{sh} = \frac{\pi}{4}\rho|\overline{V}_h - \overline{V}_s|\overline{E}_{sh}N_sN_h\lambda_h^{-2}[(\lambda_hD_*)^2 + 2\lambda_hD_* + 2 + 4\frac{\lambda_h}{\lambda_s}(\lambda_hD_* + 1) + 6(\frac{\lambda_h}{\lambda_s})^2], \tag{11}$$

$$NC_{gh} = \frac{\pi}{4}\rho|\overline{V}_h - \overline{V}_g|\overline{E}_{gh}N_gN_h\lambda_h^{-2}[(\lambda_hD_*)^2 + 2\lambda_hD_* + 1 + 2\frac{\lambda_h}{\lambda_g}(\lambda_hD_* + 1) + 2\left(\frac{\lambda_h}{\lambda_g}\right)^2], \tag{12}$$

Where $C_{ch}, C_{rh}, C_{ih}, C_{sh}, C_{gh}$ (g kg^{-1} s^{-1}) are mass collision rate of cloud, rain, ice, snow, and graupel to hail, respectively.

95    $NC_{rh}, NC_{ih}, NC_{sh}, NC_{gh}$ (kg^{-1} s^{-1}) are number collision rate of rain, ice, snow, and graupel to hail, respectively. $\overline{V}_r, \overline{V}_i, \overline{V}_s$,

$\overline{V}_g$ (cm s^{-1}) are mean fall speed of rain, ice, snow, and graupel, respectively. Note that the mean fall speed of those

hydrometeors can be calculated using equations similar to Eq. (3), which can be seen in Hu and He (1988). $\overline{E}_{ch}, \overline{E}_{rh}, \overline{E}_{ih}$,

$\overline{E}_{sh}, \overline{E}_{gh}$ is the collision coefficient of cloud, rain, ice, snow, and graupel to hail, respectively, which is 0.8 in this study. λ_r,

$\lambda_i, \lambda_s, \lambda_g$ (cm) is the slope parameter for rain, ice, snow, and graupel, respectively.

100   Autoconversion, melting, and sublimation processes of hail are list below:

$$A_{gh} = Aexp(-\lambda_gD_{*g})\left[1 + \lambda_gD_{*g} + \frac{1}{2}(\lambda_gD_{*g})^2 + \frac{1}{6}(\lambda_gD_{*g})^3\right]Q_g, \tag{13}$$

$$NA_{gh} = Aexp(-\lambda_gD_{*g})N_g, \tag{14}$$

Where A_{gh} (g kg^{-1} s^{-1}) and NA_{gh} (kg^{-1} s^{-1}) are mass and number autoconversion rates of graupel to hail, A is the conversion

parameter, which is 0.01 s^{-1}, D_{*g} (cm) is the diameter of graupel, which is 0.97.

105   $$M_{hr} \approx \frac{0.58\pi}{L_f}\sqrt{\frac{A_{vh}\rho}{\mu}}[k_t(T - T_0) + L_vk_d\rho(Q_v - Q_{s0})]N_h\lambda_h^{-1.9}[(\lambda_hD_*)^{1.9} + 1.8274(0.9\lambda_hD_* + 1)] + \frac{C_w}{L_f}（C_{ch} + C_{rh}）$$

$$(T - T_0), \tag{15}$$

$$NM_{hr} = \frac{M_{hr}}{Q_h} * N_h, \tag{16}$$

Where M_{hr} (g kg^{-1} s^{-1}) and NM_{hr} (kg^{-1} s^{-1}) are mass and number melting rates of hail, L_f, and L_v are the latent heat of

freezing and evaporation, C_w is the specific heat capacity of water, k_t, k_d, and μ are thermal conductivity, diffusion

110   coefficient, and dynamic viscosity of water vapor, respectively. T (K) is temperature, Q_v (g kg^{-1}) is the mass mixing ratio of

water vapor, while T_0 and Q_{s0} are the temperature and saturated specific humidity of the freezing point.

$$S_{vh} = \left\{2\pi k_d\rho(Q_v - Q_{si})0.2\sqrt{\frac{A_{vh}\rho}{\mu}}N_h\lambda_h^{-1.9}[(\lambda_hD_*)^{1.9} + \Gamma(2.9)(0.9\lambda_hD_* + 1)] - \frac{L_fk_d\rho Q_{si}}{k_tT}\left(\frac{L_s}{RT} - 1\right)(C_{ch} + C_{rh})\right\}[1 +$$

$$\frac{L_fk_d\rho Q_{si}}{k_tT}\left(\frac{L_s}{RT} - 1\right)]^{-1}, \tag{17}$$

Where S_{vh} (g kg^{-1} s^{-1}) is the sublimation rate of hail, Q_{si} is the saturated specific humidity over ice, R is the universal gas

115   constant.

3 The observed hailstorm and Experimental design

3.1 The observed squall line hailstorm

A severe convective weather process occurred on June 13 2018 in Northern China. Started on June 12 2018 afternoon, a strong squall line hit the southern part of Inner Mongolia, Shanxi, Hebei, Beijing, and Shandong provinces. Fig. 1 shows the
120 hazardous weather (heavy precipitation and strong wind) reported in Northern China, and hail disaster reported in Shandong province from 0000 UTC 13 June 2018 to 0000 UTC 14 June 2018. This process reported a wicked wind speed around 20 m s^{-1}, and a maximum wind speed of 34.8 m s^{-1} in Qingdao city, along with hourly rainfall rates even over 50 mm h^{-1}. The blue triangles indicate the locations where hailstones were observed, the typical hailstone diameter in this process is around 5-20 mm in this hailstorm, and even higher than 20 mm were recorded. The associated hailstorm caused significant casualties and
125 economic losses. Nearly 860,000 people were affected, 2 deaths and 1 missing, more than 4100 houses were damaged. The damaged area of crops is 105, 800 m^2, and the direct economic loss is almost 1 billion yuan.

The synoptic-scale background associated with this squall line hailstorm is shown in Fig. 2. At 0600 UTC on 13 June 2018, the atmospheric circulation at 500 hPa was characterized by a cold vortex that came from the northeast over the north China plain, as shown in Fig. 2b. Shandong province was located at the bottom of the cold vortex and in the region ahead of the
130 East Asian trough (EAT), where is favorable for upward vertical motion, as shown in Fig. 2a, b. Meanwhile, a warm low existed in the north China plain. The strong midlevel cold air advection from the north was superimposed on low-level warm advection from the south in this region, leading to destabilization of the atmosphere, as shown in Fig. 2c, d. At 1000 hPa, there was noticeable wind convergence along the cold front in Shandong province, as shown in Fig. 2e.

A Skew-T plot with hodograph was used to analyze the stratification of the atmosphere at Qingdao Station at 0000 UTC on
135 13 June 2018 (9 h before the hailstorm passed by), as shown in Fig. 3. The sounding of radiosonde data is from the University of Wyoming. Relatively cold air between 250 and 650 hPa contributes to convective available potential energy (CAPE) of 1022.59 J kg^{-1}, with convective inhibition (CIN) of 541.02 J kg^{-1} in this sounding. The CAPE is suitable for the formation of deep convection. CIN was quite big compared to other hailstorms (Luo et al., 2014; Yin et al., 2019), this might because it needed 9 hours before the hailstorm passed. From surface to 850 hPa, horizontal wind changes from southeasterly
140 to westerly. There is a wind shear above the free convection level (LFC, around 3000 m), which provided a suitable condition for hail growth (Dennis and Matthew, 2017). The wind speed increased with height and can be 20 m s^{-1} at around 8000 m. Meanwhile, the dew point profile shows a clear mixing of the wet and dry layers in the middle troposphere, which is favorable for the growth of hail (Luo et al., 2014; Costa et al., 2001; Webb and Muirhead, 2002).

3.2 Experimental design

145 This study uses GRAPES_Meso (version 4.4) to simulate the squall line hailstorm. The modified double-moment microphysics scheme is used to simulate the cloud microphysical processes. The Medium-Range Forecast (MRF) scheme (Hong and Pan, 1996) is used to parameterize the boundary-layer processes. The rapid radiative transfer model (RRTM)

scheme (Mlawer et al. 1997) and Dudhia scheme (Dudhia 1989) are adopted to parameterize the longwave and shortwave

radiative transfer process, respectively. The cumulus process is closed in this study. Fig. 1 also implies the simulation

150 domain, which covers the Shandong province. The initial and boundary conditions are supplied by the 0.5º National Centers

for Environmental Prediction (NCEP) 6-h reanalysis data. The horizontal resolution is 0.03º, and the vertical resolution

increases toward the model top at 35000 m. The simulation period starts at 1800 UTC on June 12 2018 and runs for 24 hours

to simulate the squall line hailstorm.

4 Results

4.1 Accumulated precipitation
155

Fig. 4 shows four hours of accumulated precipitation from 0080 to 1100 UTC 13 June 2018 for observation and simulation.

This period covers the lifetime of this squall line hailstorm. As clearly in Fig. 4, rain belts in both observation and simulation

show a southeast-northwest orientation with the maximum at around 40-100 mm. The narrow rain belt pattern also indicates

that this simulation captured this squall line successfully. However, the maximum precipitation area located east southward

160 than the observation, as shown in Fig. 4b.

4.2 Evolution of the squall line hailstorm

Composite reflectivity of four moments with 1h interval from 0080 to 1100 UTC 13 June 2018 is shown in Fig. 5a, c, e, g,

which implies the evolution of the squall line hailstorm. During the four hours, the squall line hailstorm formatted and

moved from southern to northern of Shandong province, with a southeast-northwest orientation. The squall line has a high

165 composite reflectivity. Most of its eastern part is at around $50 – 60$ dBZ, the maximum composite reflectivity of this squall

line can even up to 70 dBZ. Simulated composite reflectivity also shows a southeast-northwest orientation and northern

movement, as shown in Fig. 5b, d, f, h. The high composite reflectivity region is at around $50 – 60$ dBZ, locates at the

eastern part, and the simulated maximum composite reflectivity is up to 70 dBZ as well. Although the specific location of the

squall line is northern than that of the observation, results can still imply that this squall line is well captured by simulation

170 with GRAPES_Meso. The detail of the evolution of this squall line hailstorm is analyzed below.

As discussed in Yin et al. (2019) and Luo et al. (2014), hailstorm evolution can be separated into the stages of developing,

mature, and dissipating. Fig. 6, 7 show the cross-sections of microphysical and dynamical properties of the simulated squall

line hailstorm along the dashed lines in Fig. 5. Fig. 6 shows the mixing ratios of hail and rain shaded contours of radar

reflectivity. Fig. 7 shows the wind vector over the shaded contours of vertical velocity.

175 The radar reflectivity evolves quickly from 0800 to 0900 UTC 13 June 2018 during the developing stages of the squall line

hailstorm. As shown in Fig. 6a, the cross-section of radar reflectivity shows a convective storm with a maximum value of

over 45 dBZ at the right convective core right below 600 hPa with the temperature around 0 ℃. At this time, the mixing

ratio of hail and rain mixing ratio is up to 1 g kg^{-1} at the convective storm, as shown in Fig. 6a. This convective storm has a

strong updraft above the convective core, with a maximum vertical velocity up to 8 m s^{-1} at the cloud top. The convergence

180 and divergence of wind vector can be seen at the convective core and the top of the cloud, respectively. The convective storm has a large anvil at around 200-400 hPa, and the mixing ratio of total cloud hydrometeors in the convective storm is around 2 g kg^{-1} at the convective core, as shown in Fig. 7a.

As the squall line hailstorm developed, the convective storm enhanced with a maximum radar reflectivity of 60 dBZ, the maximum mixing ratio of hail increased to 4 g kg^{-1} at the convective core, the mixing ratio of rain also increased, as shown

185 in Fig. 6b. The vertical velocity increased to over 12 m s^{-1} at the convective core. The region of high vertical velocity (> 4 m s^{-1}) thickened, from near ground to the top of the cloud. Downdraft also enhanced at the convective core from 600-800 hPa. The convergence of the wind vector is clear at this time, and the mixing ratio of total cloud hydrometeors is more than 4 g kg^{-1} in the convective core, as shown in Fig. 7b.

The mature stage of the squall line hailstorm can be seen at 1000 UTC 13 June 2018. The convective storm continued

190 enhanced with a maximum radar reflectivity near 70 dBZ. The mixing ratio of hail is over 8 g kg^{-1} in the convective core. The high radar reflectivity and large mixing ratio of hail near the ground imply large hailstones are falling to the ground at this stage of the hailstorm, as also mentioned by Luo et al. (2014). The mixing ratio of rain near the ground increased implies that there was heavy precipitation at this time as well, as shown in Fig. 6c. The dynamic field also shows a strong updraft with a maximum value of over 12 m s^{-1} in the convective core. The convergence of wind vector is still clear, and the total

195 cloud hydrometeors mixing ratio is more than 8 g kg^{-1} in the convective core, as shown in Fig. 7c.

The squall line hailstorm dissipated rapidly with a decreasing maximum radar reflectivity of only 40 dBZ in the convective core. The mixing ratio of rain at the bottom of the cloud is small at this time, as shown in Fig. 6d. The mixing ratio of total cloud hydrometeors is down to 2 g kg^{-1}. No noticeable updraft and downdraft at this stage, convergence, and divergence are also decreasing, as can be seen in Fig. 7d.

200 To be more specific, the profiles of cloud hydrometeors are shown in Fig. 8. Those profiles are plotted at the red cross along the dashed line in the right column. As already mentioned above, the simulated squall line hailstorm evolved from 0800 – 1100 UTC 13 June 2018. The squall line hailstorm started to produce hail at around 0800 UTC 13 June 2018. The maximum mixing ratio of hail is around 1 g kg^{-1} at around 600 hPa at this time. Rain fell to the ground, with a maximum mixing ratio over 2 g kg^{-1} near the surface, as shown in Fig. 8b. The mixing ratio of hail increases as the storm is enhanced. At 0900 UTC

205 13 June 2018, the maximum mixing ratio of hail is 2 g kg^{-1}, other mixing ratios of cloud hydrometeors also increased, as well as the mixing ratio of rain near the surface, as shown in Fig. 8d. The mixing ratio of hail and rain reach their maximum at 1000 UTC 13 June 2018, with a maximum of 4 and 7 g kg^{-1} respectively. A large amount of hail and rain hit the ground at this time, as shown in Fig. 8f. The squall line hailstorm passes and dissipated at 1100 UTC 13 June 2018. The mixing ratio of rain near the surface weakened as well, as shown in Fig. 8h.

210 The basic characteristics of the development of a hailstorm are consistent with previous studies (Luo et al. 2014; Ying et al. 2019). Those results point out that the squall line hailstorm is well captured using the modified double-moment microphysical scheme in GRAPES_Meso.

4.3 Hail microphysical processes and cloud properties in the hailstorm

Two hailstorms are chosen to investigate the validity of the modified double-moment microphysics scheme in detail, despite
215 the location and time error between observation and simulation. Fig. 9a shows the cross-section of operational radar
reflectivity of a deep convective cloud at 1000 UTC 13 June 2018 at Qingdao city. The maximum reflectivity can be over 70
dBZ at around 500 hPa. There is a thick high-value area of reflectivity (>40 dBZ) from the surface to around 200 hPa in this
deep convective cloud, such high reflectivity implies heavy precipitation at this time. Note that the blank area below 930 hPa
is because of the lack of data. The large area of radar reflectivity around 30 dBZ at 200-600 hPa also implies the large cloud
220 anvil of this deep convective cloud. Fig. 9b shows the cross-section of simulated radar reflectivity of a deep convective
cloud at 0940 UTC 13 June 2018 at around (38.25 ºS, 120.8 ºN). The maximum reflectivity is near 70 dBZ at around 600
hPa, which is slightly lower than that of the observation. The high-value area of reflectivity (>40 dBZ) is from the surface to
around 200 hPa as well. The maximum mixing ratio of hail is over 4 g kg^{-1} at the convective core. It can be seen at this time,
simulated hail fell to the ground, and this deep convective cloud produces a large amount of precipitation. The simulated
225 convective cloud also contains a large cloud anvil, as shown in Fig. 9b. Results show that the basic characteristic of the deep
convective cloud is well captured using the modified double-moment microphysical scheme in GRAPES_Meso, compare to
the observation.

To be more specific, the hail production rate of the simulated deep convective cloud is analyzed in Fig. 10. The hail
production rate of collision processes, autoconversion, melting, and sublimation are shown in Fig. 10a, b, c, d, respectively.
230 It can be seen that autoconversion and melting processes are the dominant source and sink terms in hail production. The
maximum hail production rate can be over 1e-5 g kg^{-1} s^{-1} for these two terms, which is consistent with a previous study (Hu
and He et al., 1989). The collision and autoconversion processes are much active below 0 ℃, as shown in Fig. 10a, b. It can
be seen that graupel is the most important source of hail production in this modified double-moment scheme. The melting
process is also very active, the falling hailstones melted to rain above 0 ℃, as shown in Fig. 10c. The results are consistent
235 with Fig. 9e, f, which shows a hailstorm in its mature stage. Moreover, it can be seen that the sublimation process evaporated
hail to water vapor, and moistures the environment, as shown in Fig. 10d.

5 Summary and Discussion

A severe squall line hailstorm is simulated using a modified double-moment microphysics scheme in high-resolution
GRAPES_Meso that occurred on 13 June 2018. This squall line hailstorm caused strong wind, heavy precipitation, and hail
240 reported on most of the Shandong province. Simulation results of accumulated precipitation, radar reflectivity, and cloud
hydrometeor properties were compared to observation. The detailed mechanism of hail production in the modified double-
moment microphysics scheme was analyzed. The major points of this study are noted as follows:
The squall line hailstorm occurred in a synoptic environment with a strong midlevel cold air advection from the north and
was superimposed on low-level warm advection from the south, leading to destabilization of the atmosphere in Shandong

Geoscientific
Model Development
Discussions

245   province. The CAPE is quite high at 1022 J kg⁻¹. There is a mixing of the wet and dry layers in the middle troposphere, which is favorable for hail formation.

Compared to the observed accumulated precipitation and radar reflectivity, simulation results of GRAPES_Meso with the modified double-moment microphysical scheme generally reproduced the development of this squall line hailstorm, although there might be time and location errors.

250   The cross-section of the dynamic, microphysical, and radar reflectivity structures of the simulated hailstorm was analyzed. The development of this hailstorm is consistent with previous studies of hailstorms (Luo et al., 2014; Ying et al., 2019). The profiles of cloud hydrometeors in the hailstorm are analyzed, the distribution is also reasonable.

Detailed analysis of hail production rate shows that the formation and growth of hail are reasonable and consistent with the previous study (Hu and He, 1989), which implies the modified double-moment microphysical can successfully predict

255   hailstorm in GRAPES_Meso.

260

Author contribution. ZL, QJL, and ZSM designed the experiments and ZL carried them out. ZL modified the model code based on XMC's version and performed the simulations. ZL prepared the manuscript with the contributions of all co-authors.

Competing interests. The authors declare that they have no conflict of interest.

References

Adams-Selin, R. D., and Ziegler, C. L.: Forecasting Hail Using a One-Dimensional Hail Growth Model within WRF, Mon
270   Weather Rev, 144, 4919-4939, https://doi.org/10.1175/Mwr-D-16-0027.1, 2016.

Bringi, V. N., Vivekanandan, J., and Tuttle, J. D.: Multiparameter Radar Measurements in Colorado Convective Storms. Part
II: Hail Detection Studies, J Atmos Sci, 43, 2564–2577, https://doi.org/10.1175/1520-
0469(1986)043<2564:MRMICC>2.0.CO;2, 1986.

Browning, K. A.: The Growth of Large Hail within a Steady Updraught, Q J Roy Meteor Soc, 89, 490-506,
275   https://doi.org/10.1002/qj.49708938206, 1963.

Cao, Z. H.: Severe hail frequency over Ontario, Canada: Recent trend and variability, Geophys Res Lett, 35,
    https://doi.org/10.1029/2008GL034888, 2008.

Chen, X. M., Liu, Q. J., and Zhang, J. C.: A Numerical Simulation Study on Microphysical Structure and Cloud Seeding in
    Cloud System of Qilian Mountain Region, Meteor. Mon., 33, 33-43, https://doi.org/10.3969/j.issn.1000-
280   0526.2007.07.004, 2007 (in Chinese).

Chen, D. H., Xue, J. X., Shen, X. S., Sun, J., Wan, Q. L., Jin, Z. Y., and Li, X. L.: Application and prospect of a new
    generation of numerical weather prediction system (GRAPES), Eng Sci, 14, 46-54, 2012 (in Chinese).

Chen, J., Ma, Z. S., Li, Z., Shen, X. S., Su, Y., Chen, Q. Y., and Liu, Y. Z.: Vertical diffusion and cloud scheme coupling to
    the Charney-Phillips vertical grid in GRAPES global forecast system, Q J Roy Meteor Soc, 146, 2191-2204,
285   https://doi.org/10.1175/JAS-D-15-0099.1, 2020.

Costa, S., Mezzasalma, P., Levizzani, V., Alberoni, P. P., and Nanni, S.: Deep convection over Northern Italy: synoptic and
    thermodynamic analysis, Atmos Res, 56, 73-88, https://doi.org/10.1016/S0169-8095(00)00091-0, 2001.

Das, P.: Influence of Wind Shear on the Growth of Hail, J Atmos Sci, 19, 407-414, https://doi.org/10.1175/1520-
    0469(1962)019<0407:IOWSOT>2.0.CO;2, 1962.

290   Deng, H., Xue, J. X., Xu, H. M., and He, J. H.: Study of Different Cumulus Parameterization Schemes of GRAPES_Meso
    Model in Simulation of Convection Provocation, J. Trop. Meteor., 24, 327-334, https://doi.org/10.3969/j.issn.1004-
    4965.2008.04.003, 2008 (in Chinese).

Dennis, E. J., and Kumjian, M. R.: The Impact of Vertical Wind Shear on Hail Growth in Simulated Supercells, J Atmos Sci,
    74, 641-663, https://doi.org/10.1175/Jas-D-16-0066.1, 2017.

295   Dudhia, J.: Numerical Study of Convection Observed during the Winter Monsoon Experiment Using a Mesoscale Two-
    Dimensional Model, J Atmos Sci, 46, 3077-3107, https://doi.org/10.1175/1520-
    0469(1989)046<3077:NSOCOD>2.0.CO;2, 1989.

Fu, L., Li, W. J., Zhang, P. Q., Zhang, Q., and Gao, G.: Inter-Decadal Change of Hail Events over China and Causation
    Analysis in Northern China in Recent 50 Years, Meteor. Mon., 37, 669-676, https://doi.org/10.7519/j.issn.1000-
300   0526.2011.6.003, 2011 (in Chinese).

García-García, F., and List, R.: Laboratory Measurements and Parameterizations of Supercooled Water Skin Temperatures
    and Bulk Properties of Gyrating Hailstones, J Atmos Sci, 49, 2058-2073, https://doi.org/10.1175/1520-
    0469(1992)049<2058:LMAPOS>2.0.CO;2, 1992.

Hong, S. Y., and Pan, H. L.: Nonlocal Boundary Layer Vertical Diffusion in a Medium-Range Forecast Model, Mon
305   Weather Rev, 124, 2322-2339, https://doi.org/10.1175/1520-0493(1996)124<2322:NBLVDI>2.0.CO;2, 1996.

Hu, Z. J., and He, G. F.: Numerical simulation of microphysical processes in cumulonimbus Part (I): Microphysical model, J
    Meteorol Res-Prc, 2, 471-489, 1988.

Hu, Z. J., and He, G. F.: Numerical simulation of microphysical processes in cumulonimbus Part (II): Case Studies of Shower, Hailstorm and Torrential Rain, J Meteorol Res-Prc, 3, 1989.

310 Hu, Z. J., and Yan, C. F.: Numerical simulation of microphysical processes in stratiform clouds(I) Microphysical model, Annual Report of Academy of Meteorological Science, SMA., 1, 37-52, 1986 (in Chinese).

Huang, L. P., Chen, D. H., and Ma, M.: The GRAPES high resolution mesoscale lightning forecast model and its preliminary validation, J Meteorol Res-Prc, 70, 291-301, 2012 (in Chinese).

Hubbert, J., Bringi, V. N., Carey, L. D., and Bolen, S.: CSU-CHILL Polarimetric Radar Measurements from a Severe Hail

315 Storm in Eastern Colorado, J. Appl. Meteorol., 37, 749-775, https://doi.org/10.1175/1520-0450(1998)037<0749:CCPRMF>2.0.CO;2 1998.

Ilotoviz, E., Khain, A. P., Benmoshe, N., Phillips, V. T. J., and Ryzhkov, A. V.: Effect of Aerosols on Freezing Drops, Hail, and Precipitation in a Midlatitude Storm, J Atmos Sci, 73, 109-144, https://doi.org/10.1175/Jas-D-14-0155.1, 2016.

Jewell, R., and Brimelow, J.: Evaluation of Alberta Hail Growth Model Using Severe Hail Proximity Soundings from the

320 United States, Weather Forecast, 24, 1592-1609, https://doi.org/10.1175/2009waf2222230.1, 2009.

Knight, C., Knight, N., and Brooks, H. E.: MESOSCALE METEOROLOGY | Hail and Hailstorms, Encyclopedia of Atmospheric Sciences (Second Edition), 334-338, https://doi.org/10.1016/B978-0-12-382225-3.00482-5, 2015.

Kunz, M., Sander, J., and Kottmeier, C.: Recent trends of thunderstorm and hailstorm frequency and their relation to atmospheric characteristics in southwest Germany, Int J Climatol, 29, 2283-2297, https://doi.org/10.1002/joc.1865,

325 2009.

Labriola, J., Snook, N., Jung, Y., and Xue, M.: Explicit Ensemble Prediction of Hail in 19 May 2013 Oklahoma City Thunderstorms and Analysis of Hail Growth Processes with Several Multimoment Microphysics Schemes, Mon Weather Rev, 147, 1193-1213, https://doi.org/10.1175/Mwr-D-18-0266.1, 2019.

Lesins, G. B., and List, R.: Sponginess and Drop Shedding of Gyrating Hailstones in a Pressure-Controlled Icing Wind

330 Tunnel, J Atmos Sci, 43, 2813-2825, https://doi.org/10.1175/1520-0469(1986)043<2813:SADSOG>2.0.CO;2, 1986.

Li, Z., Zhang, Y. T., Liu, Q. J., Fu, S. Z., and Ma, Z. S.: A Study of the Influence of Microphysical Processes on Typhoon Nida (2016) using a New double-moment Microphysics Scheme in the Weather Research and Forecasting Model, J. Trop. Meteor., 24, 123-130, https://doi.org/10.16555/j.1006-8775.2018.02.001, 2018.

Li, Z., Liu, Q. J., Ma, Z. S., Chen, J., and Jiang, Q. G.: Simulation Study of Cloud Properties Affected by Heterogeneous

335 Nucleation Using the GRAPES_SCM during the TWP-ICE Campaign, J Meteorol Res-Prc, 33, 734-746, https://doi.org/10.1007/s13351-019-8203-1, 2019.

Li, Z., Ma, Z. S., Liu, Q. J., and Yang, Y. L.: The improvement of GRAPES double moment cloud scheme and case study of cloud precipitation Part I: modeling study of tropical convective cloud via GRAPES_SCM, Meteor. Mon., 45, 756-765, https://doi.org/10.7519/j.issn.1000-0526, 2019 (in Chinese).

340   Luo, L. P., Xue, M., Zhu, K. F., and Zhou, B. W.: Explicit prediction of hail using multimoment microphysics schemes for a hailstorm of 19 March 2014 in eastern China, J Geophys Res-Atmos, 122, 7560-7581, https://doi.org/10.1002/2017jd026747, 2017.

Ma, Z. S., Liu, Q. J., Zhao, C. F., Shen, X. S., Wang, Y., Jiang, J. H., Li, Z., and Yung, Y.: Application and Evaluation of an Explicit Prognostic Cloud-Cover Scheme in GRAPES Global Forecast System, J Adv Model Earth Sy, 10, 652-667,
345   https://doi.org/10.1002/2017ms001234, 2018.

Ma, Z., Zhao, C., Gong, J., Zhang, J., Li, Z., Sun, J., Liu, Y., Chen, J., and Jiang, Q.: Spin-up Characteristics with Three Types of Initial Fields and the Restart Effects on the Forecast Accuracy in GRAPES Global Forecast System, https://doi.org/10.5194/gmd-2020-177, inreview, 2020.

Mlawer, E. J., Taubman, S. J., Brown, P. D., Iacono, M. J., and Clough, S. A.: Radiative Transfer for Inhomogeneous
350   Atmospheres: RRTM, a Validated Correlated-K Model for the Longwave, J. Geophys. Res.-Atmos., 102, 16663-16682, http://dx.doi.org/10.1029/97JD00237, 1997.

Mohr, S., and Kunz, M.: Recent trends and variabilities of convective parameters relevant for hail events in Germany and Europe, Atmos Res, 123, 211-228, https://doi.org/10.1016/j.atmosres.2012.05.016, 2013.

Moore, J. T., and Pino, J. P.: An Interactive Method for Estimating Maximum Hailstone Size from Forecast Soundings,
355   Weather Forecast, 5, 508-526, https://doi.org/10.1175/1520-0434(1990)005<0508:AIMFEM>2.0.CO;2, 1990.

Shi, R. G., Liu, Q. J., and Ma, Z. S.: Numerical simulation of aerosol effects on cloud and precipitation using GRAPES model, Meteor. Mon., 41, 272-285, https://doi.org/10.7519/j.issn.1000-0526.2015.03.002, 2015 (in Chinese).

Sokol, Z., Zacharov, P., and Skripnikova, K.: Simulation of the storm on 15 August, 2010, using a high resolution COSMO NWP model, Atmos Res, 137, 100-111, https://doi.org/10.1016/j.atmosres.2013.09.015, 2014.

360   Vie, B., Pinty, J. P., Berthet, S., and Leriche, M.: LIMA (v1.0): A quasi two-moment microphysical scheme driven by a multimodal population of cloud condensation and ice freezing nuclei, Geosci Model Dev, 9, 567-586, https://doi.org/10.5194/gmd-9-567-2016, 2016.

Wan, Z. W., Wang, J. J., Huang, L. P., and Kang, J. Q.: An improvement of the shallow convection parameterization scheme in the GRAPES-Meso, J Meteorol Res-Prc, 6, 1066-1079, https://doi.org/10.11676/qxxb2015.071, 2015.

365   Wang, J. C., Gong, J. D., and Deng, L. T.: Operational Assimilation of Data Retrieved by GNSS Observations into GRAPES_Meso 3DVar System, J. Appl. Meteor. Sci., 6, 654-668, 2014 (in Chinese).

Wang, L. L., Chen, D. H., Bao, H. J., and Zhang, K.: On simulation improvement of the Noah_LSM by coupling with a hydrological model using a double-excess runoff production scheme in the GRAPES_Meso model, Meteorol Appl, 24, 512-520, https://doi.org/10.1002/met.1651, 2017.

370   Webb, J. D., and Muirhead, R.: Severe hailstorm over west Cornwall on 25 August 2000, Weather, 57, 371-374, https://doi.org/10.1256/wea.281.01, 2002.

Xu, C. L., Wang, J. J., and Huang, L. P.: Evaluation on QPF of GRAPES_Meso 4.0 model at convection-permitting resolution, 75, 851-876, https://doi.org/10.11676/qxxb2017.068, 2017 (in Chinese).

Yang, H. L., Xiao, H., and Hong, Y. C.: A numerical study of aerosol effects on cloud microphysical processes of hailstorm
375   clouds, Atmos Res, 102, 432-443, 2011.

Yin, L., Ping, F., and Mao, J. H.: Impact of cloud microphysical processes on the simulation of a hailstorm in East China,
     Atmos Res, 219, 36-56, 10.1016/j.atmosres.2018.12.014, 2019.

Zhang, J. C., and Liu, Q. J.: Analysis of Cloud Schemes in Simulation of Short-Term Climatic Process, Meteor. Mon., 32, 3-
     12, https://doi.org/10.3969/j.issn.1000-0526.2006.07.001, 2006 (in Chinese).

380 Zhao, W. H., Yao, Z. Y., Jia, S., Wang, W. J., Zhang, P., and Gao, L. S.: Characteristics of spatial and temporal distribution
     of hail duration in China during 1961-2015 and its possible influence factors, Chi. J. Atmos. Sci., 43, 539-551,
     https://doi.org/10.3878/j.issn.1006-9895.1808.18123, 2019 (in Chinese).

Figures

385   Figure 1: Hazard weather reports in Northern China from 0000 UTC 13 June 2018 to 0000 UTC 14 June 2018. Blue triangles represent hailstorms, colored circles and pentagons represent strong rainfall, strong wind respectively. The red star marks Qingdao city. Data obtained from china meteorological data service center http://data.cma.cn/. Note that the background map is a topo map that indicates the terrain height.

Figure 2: Synoptic features of (a) 200 hPa, (b) 500hPa, (c) 700 hPa, (d) 850 hPa, and (e) 1000 hPa at 0600 UTC 13 June 2018, showing
390   wind barbs, relative humidity (shaded), temperature (red dashed contours), and geopotential height (blue solid contours). Red stars mark the Qingdao city.

Figure 3: Skew -T plot and hodograph observed at Qingdao Station analysis data at 0000 UTC 13 June 2018.

Figure 4: Four hours accumulated precipitation (shaded, mm) from 0080 to 1100 UTC 13 June 2018. (a) is from observation, (b) is the simulation results. Red stars mark the Qingdao city.

395   Figure 5: Composite reflectivity (shaded, dBZ) of operational radars (a, c, e, and g) and model simulation (b, d, f, and h) from 0800 to 1100 UTC 13 June 2018 with 1-hour intervals. The solid circles represent the high reflectivity area. Red stars mark the Qingdao city. Note that there are location errors in the simulations compared to the observations. The dashed lines indicate the locations of the cross-sections in Fig. 6, 7.

Figure 6: Cross-sections of simulated radar reflectivity (shaded, dBZ) along the black dash lines in Fig. 5. Solid contours represent hail
400   mixing ratio (g kg^{-1}), dashed contours represent rain mixing ratio (g kg^{-1}) respectively. The purple lines represent the 0 and -20 isotherms.
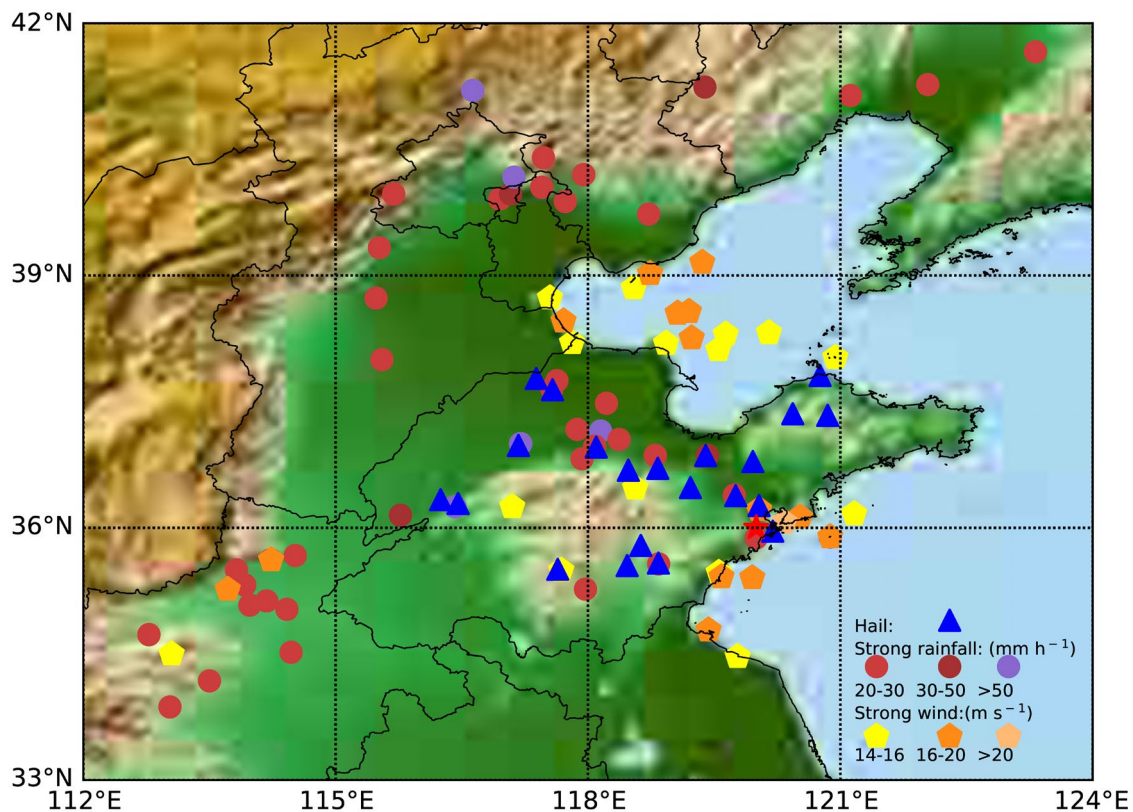
Figure 7: Same as Fig. 6. but for the vertical velocity (shaded, m s^{-1}) and wind field (vectors). Blue contours represent the sum of cloud hydrometeors mixing ratios (g kg^{-1}). The purple lines represent the 0 and -20 isotherms.

Figure 8: Profiles of cloud hydrometeors (a, c, e, and g) at the red cross along the dashed lines (b, d, f, and h, enlarged from Fig. 5) with rain mixing ratio (shaded, g kg^{-1}) at 1000 hPa and hail mixing ratio (blue contours) at 1000 hPa.
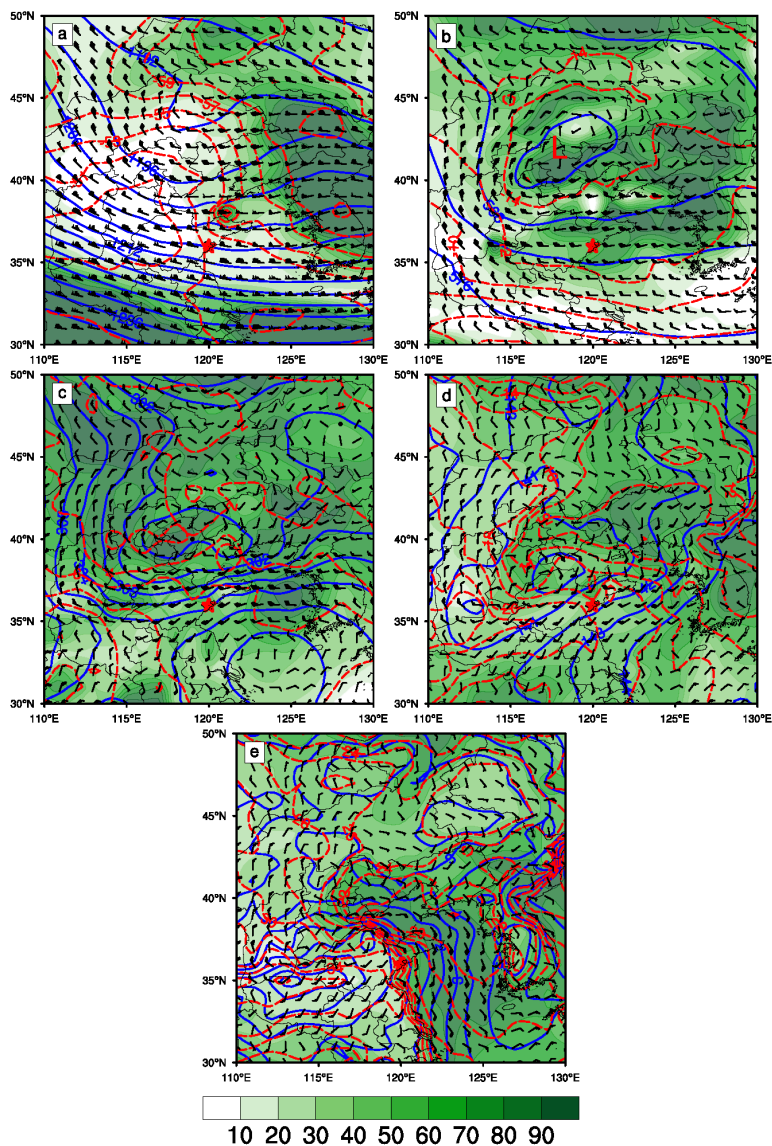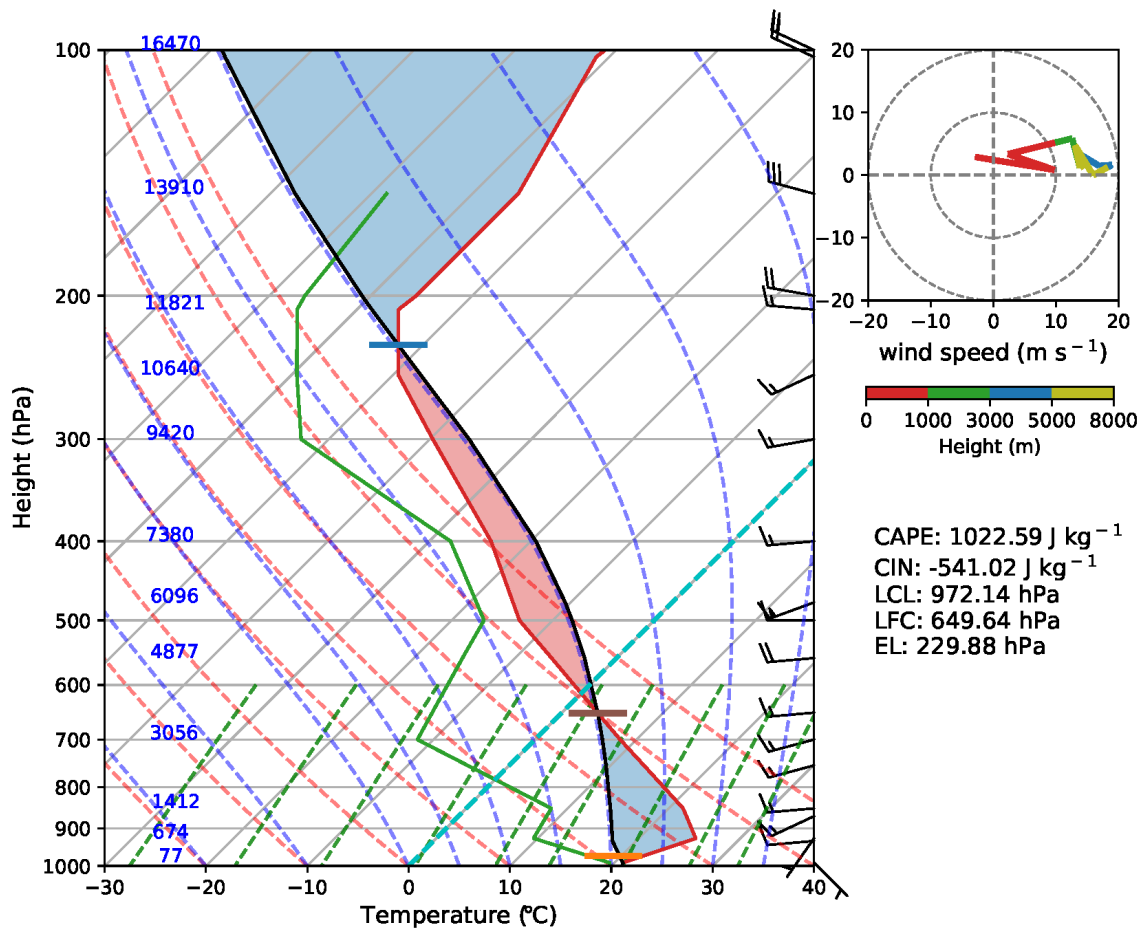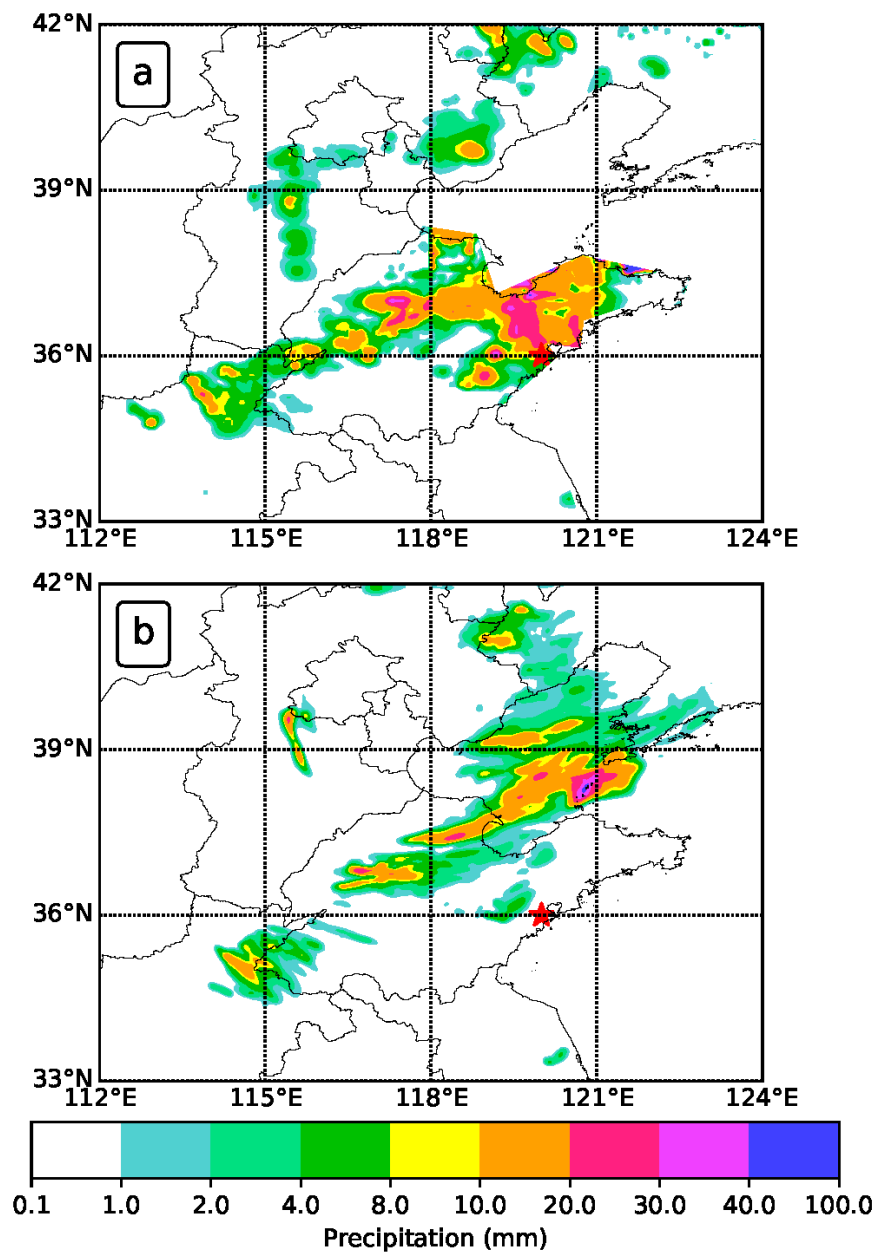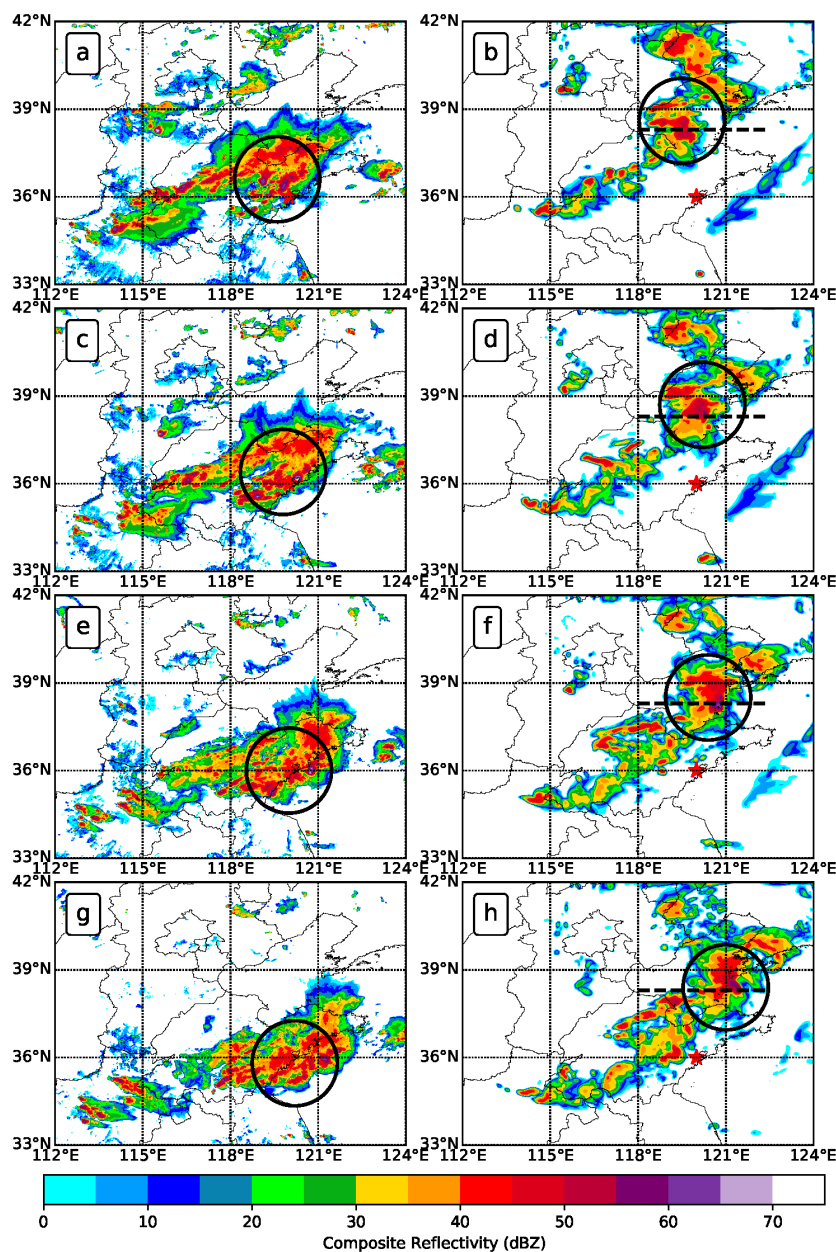
405   Figure 9: Cross-sections of radar reflectivity (dBZ) at typical strong convective core area. (a) is for operational radar at 0900 UTC 13 June 2018 at Qingdao city, (b) is simulation result at 0940 UTC June 2018 at around 38 ºS, 121 ºE. Solid contours represent hail mixing ratio (g kg^{-1}). The purple lines represent the 0 and -20 isotherms. Note that there are time and location errors in the simulation compared to the observation.

Figure 10: Same as Fig. 9. but for the hail production rate (1e-5 g kg^{-1} s^{-1}), cloud hydrometeors mixing ratio, and specific humidity. Shaded
410   colors represent hail production rate from collision (a, cch, crh, cih, csh, and cgh), autoconvesion (b, agh), melting (c, rhqh), and sublimation (d, svh) respectively. Black contours (g kg^{-1}) represent the mixing ratio of ice and snow (a), graupel (b), rain (c), and specific humidity (d). The purple lines represent the 0 and -20 isotherms.

415

Figure 1: Hazard weather reports in Northern China from 0000 UTC 13 June 2018 to 0000 UTC 14 June 2018. Blue triangles
420 **represent hailstorms, colored circles and pentagons represent strong rainfall, strong wind respectively. The red star marks Qingdao city. Data obtained from china meteorological data service center http://data.cma.cn/. Note that the background map is a topo map that indicates the terrain height.**

Figure 2: Synoptic features of (a) 200 hPa, (b) 500hPa, (c) 700 hPa, (d) 850 hPa, and (e) 1000 hPa at 0600 UTC 13 June 2018, showing wind barbs, relative humidity (shaded), temperature (red dashed contours), and geopotential height (blue solid contours). Red stars mark the Qingdao city.

Geoscientific
Model Development
Discussions

Figure 3: Skew -T plot and hodograph observed at Qingdao Station analysis data at 0000 UTC 13 June 2018.

430

Figure 4: Four hours accumulated precipitation (shaded, mm) from 0080 to 1100 UTC 13 June 2018. (a) is from observation, (b) is the simulation results. Red stars mark the Qingdao city.
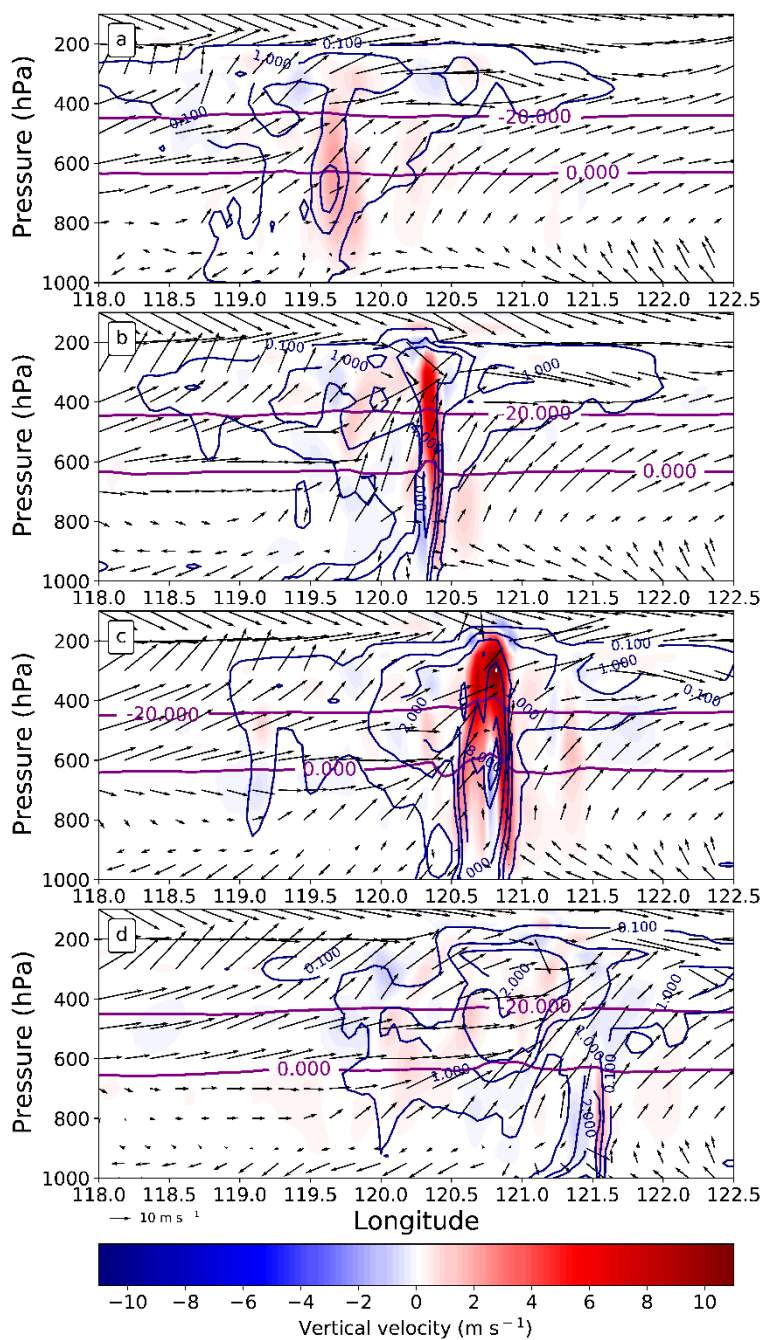
Figure 5: Composite reflectivity (shaded, dBZ) of operational radars (a, c, e, and g) and model simulation (b, d, f, and h) from 0800 to 1100 UTC 13 June 2018 with 1-hour intervals. The solid circles represent the high reflectivity area. Red stars mark the Qingdao city. Note that there are location errors in the simulations compared to the observations. The dashed lines indicate the locations of the cross-sections in Fig. 6, 7.
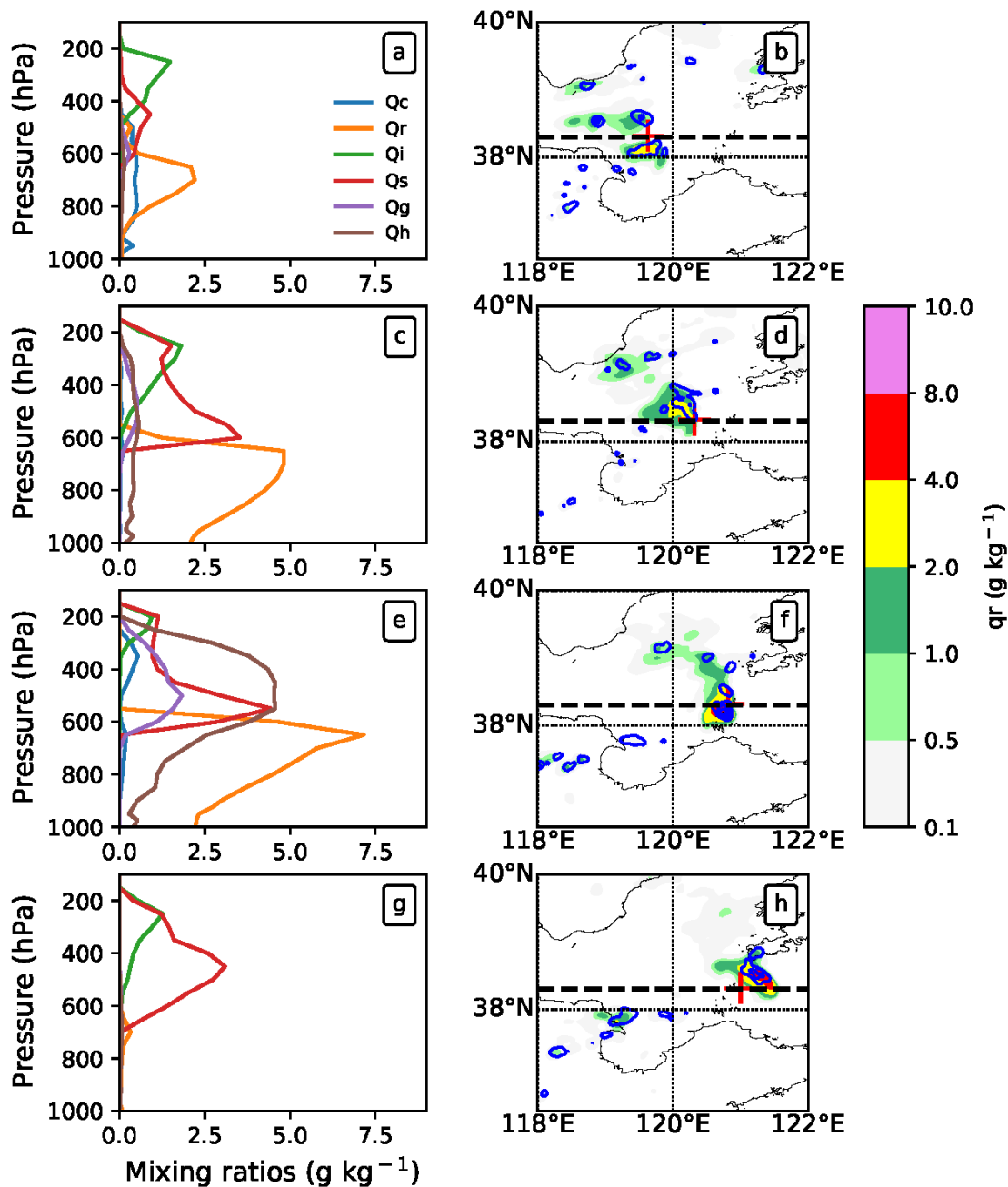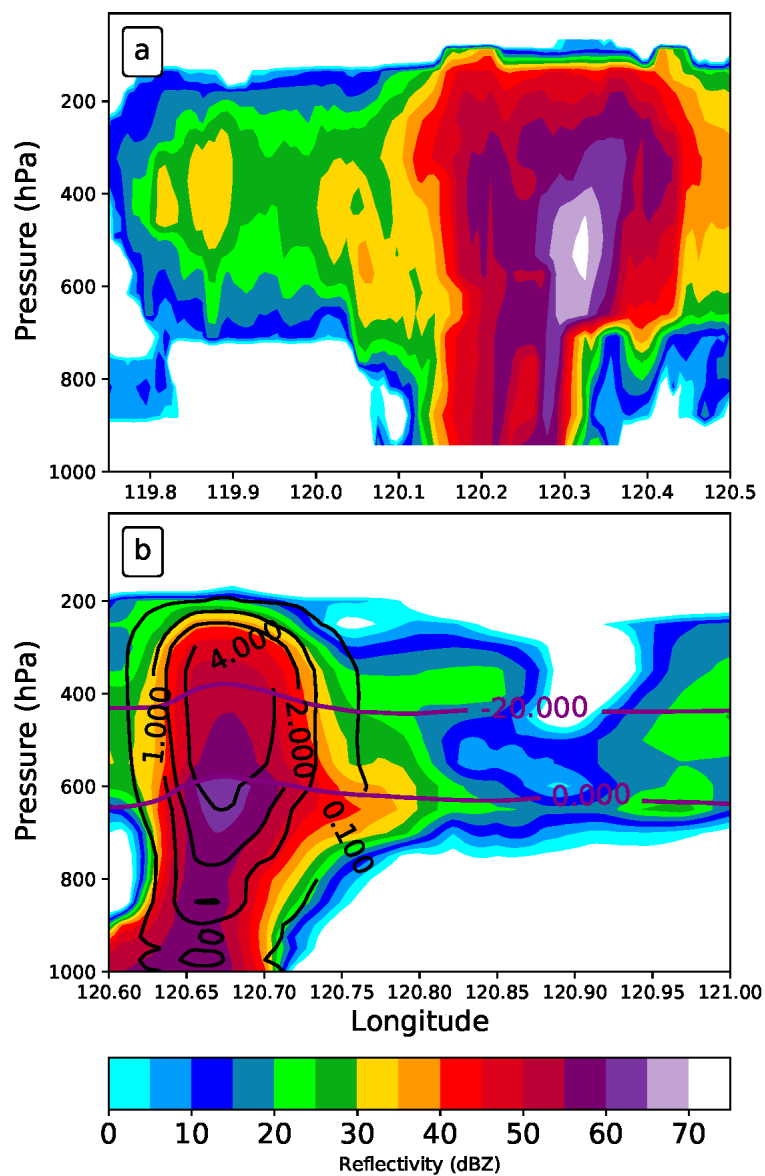
435

440

Figure 6: Cross-sections of simulated radar reflectivity (shaded, dBZ) along the black dash lines in Fig. 5. Solid contours represent hail mixing ratio (g kg⁻¹), dashed contours represent rain mixing ratio (g kg⁻¹) respectively. The purple lines represent the 0 and -20 isotherms.
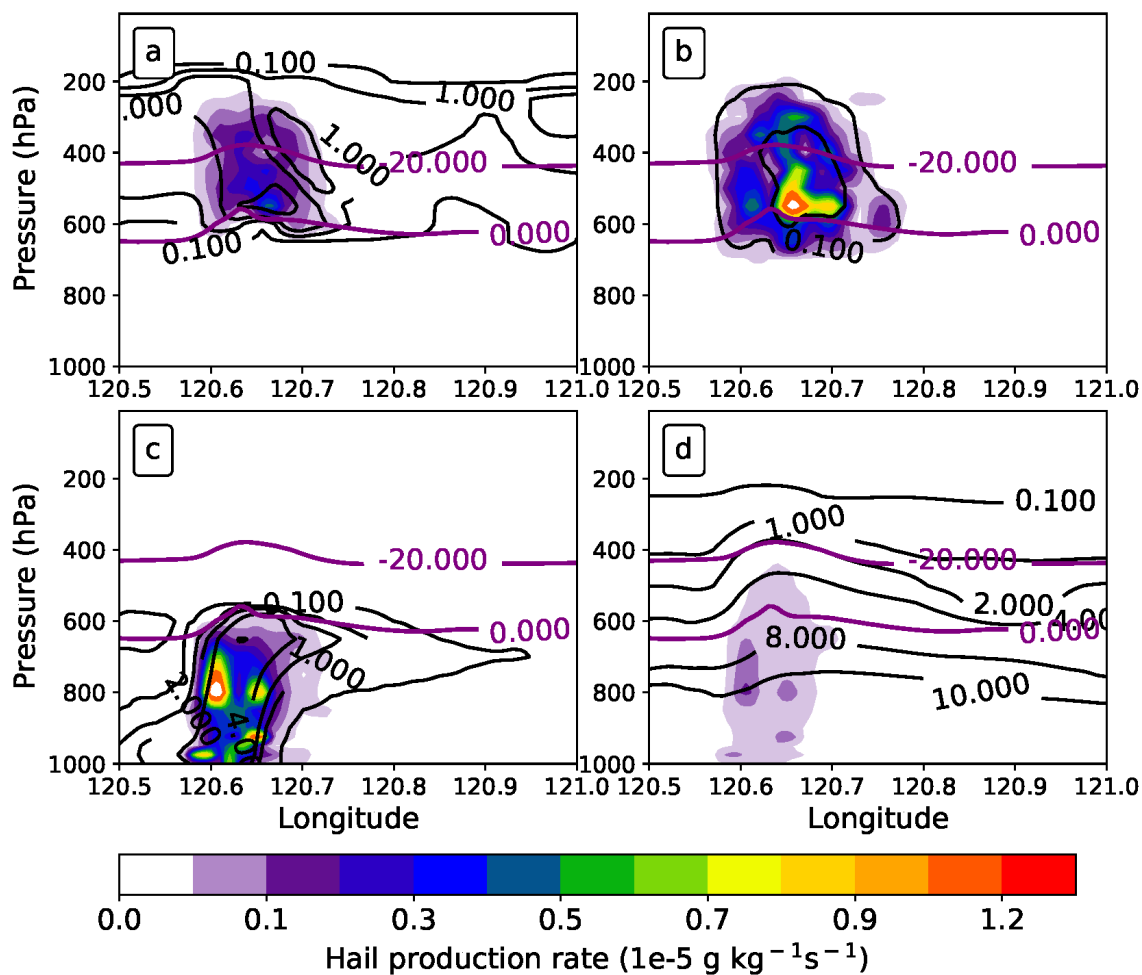
Figure 7: Same as Fig. 6. but for the vertical velocity (shaded, m s⁻¹) and wind field (vectors). Blue contours represent the sum of cloud hydrometeors mixing ratios (g kg⁻¹). The purple lines represent the 0 and -20 isotherms.

Figure 8: Profiles of cloud hydrometeors (a, c, e, and g) at the red cross along the dashed lines (b, d, f, and h, enlarged from Fig. 5)
455 **with rain mixing ratio (shaded, g kg⁻¹) at 1000 hPa and hail mixing ratio (blue contours) at 1000 hPa.**

Figure 9: Cross-sections of radar reflectivity (dBZ) at typical strong convective core area. (a) is for operational radar at 0900 UTC 13 June 2018 at Qingdao city, (b) is simulation result at 0940 UTC June 2018 at around 38 ºS, 121 ºE. Solid contours represent hail mixing ratio (g kg⁻¹). The purple lines represent the 0 and -20 isotherms. Note that there are time and location errors in the simulation compared to the observation.

Figure 10: Same as Fig. 9. but for the hail production rate (1e-5 g kg^{-1} s^{-1}), cloud hydrometeors mixing ratio, and specific humidity. Shaded colors represent hail production rate from collision (a, cch, crh, cih, csh, and cgh), autoconvesion (b, agh), melting (c, rhqh), and sublimation (d, svh) respectively. Black contours (g kg^{-1}) represent the mixing ratio of ice and snow (a), graupel (b), rain (c), and specific humidity (d). The purple lines represent the 0 and -20 isotherms.